CrossMark

A possible mechanism for the occurrence of wintertime extreme precipitation events over South China

Wenyu Huang[1] · Zifan Yang[1] · Xinsheng He[1] · Daiyu Lin[1] · Bin Wang[1,2] · Jonathon S. Wright[1] · Ruyan Chen[1] · Wenqian Ma[1] · Feifei Li[1]

Abstract

This study examines the formation of circulation patterns favorable to wintertime extreme precipitation events over South China between 1979 and 2013. During these extreme precipitation events, a barotropic wave train having seven centers of action was observed to extend from the Arabian Sea to the west coast of the North American continent with a maximum amplitude at 300 hPa. A center of action located over South China, comprised of cyclonic anomalies, favored powerful updrafts and large-scale moisture convergence over South China. About 77% of wintertime extreme precipitation events in South China were preceded by European blocking events. The formation mechanism for the 141 precipitation events with pre-existing European blocking highs is presented. Rossby wave energy propagation associated with the positive phase of circumglobal teleconnection enabled the European blocking event with a lead time of ~10 days to generate cyclonic anomalies over South China. Moreover, significant warm anomalies were present over South China before the onset of these blocking-related extreme precipitation events. Increases in atmospheric moisture holding capacity associated with these warm anomalies enabled a buildup of precipitable water via moisture fluxes into South China through the western and southern boundaries. Onset of the extreme precipitation events was then triggered by the intrusion of cold temperature anomalies from the north, which lifted warm moist air upward from the surface and lowered the moisture holding capacity, producing large amounts of precipitation.

1 Introduction

Wintertime extreme precipitation events over South China, although not as frequent as those in the other seasons (Li et al. 2005), tend to intensify the cold surges associated with the East Asian winter monsoon (Zhang et al. 1997;

✉ Wenyu Huang
huangwenyu@mail.tsinghua.edu.cn

[1] Ministry of Education Key Laboratory for Earth System Modeling, and Department of Earth System Science (DESS), Tsinghua University, Beijing 100084, China

[2] State Key Laboratory of Numerical Modeling for Atmospheric Sciences and Geophysical Fluid Dynamics (LASG), Institute of Atmospheric Physics (IAP), Chinese Academy of Sciences, Beijing 100029, China

Takaya and Nakamura 2005; Jeong and Ho 2005; Wang et al. 2010; Park et al. 2014; Leung et al. 2015). This intensification occurs through one or more of the following pathways: first, the heat in the lower troposphere is transferred to the middle troposphere through latent heat release due to condensation (Tao et al. 2001); second, the evaporation of rainwater from the land surface removes heat from the atmosphere (Trenberth et al. 2003; Trenberth 2011); third, if the lower troposphere is cold enough, precipitation will be in the form of snow, the accumulation of which increases the albedo of the land surface and inhibits the absorption of incoming short wave radiation (Shine 1984; Zhang 2005); fourth, the latent heat adsorbed by the melting of the snow from the land surface removes a large amount of heat from the lower atmosphere (Lin and Stewart 1986; Szeto et al. 1988). Since the Spring Festival and the winter vacation in China both occur in winter, the occurrence of extreme precipitation events in South China, especially those associated with heavy snowfalls, may harm the living conditions and

adversely affect the transportation activities of hundreds of millions of people (Su et al. 2011; Zhou et al. 2011; Hu et al. 2014; Xie et al. 2014). Therefore, a deeper understanding of the mechanisms behind both the occurrence and variability of extreme precipitation events could have significant societal benefit.

Many previous studies have investigated the variability of wintertime precipitation over South China from a range of perspectives. The decadal variability of the wintertime precipitation over South China was studied by Li et al. (2015), Choi et al. (2016), Jia and Ge (2017), and Huang et al. (2017). These authors recognized that the East Asia Winter Monsoon (Wang and Chen 2010; Huang et al. 2016) and sea surface temperature anomalies over the western Pacific Ocean and tropical Indian Ocean play essential roles in the decadal variations of wintertime precipitation over South China. The interannual variability of wintertime precipitation over South China has been linked to the El Niño Southern Oscillation (ENSO) (Zhou et al. 2010; Zhou and Wu 2010; Yuan et al. 2014) through the central Pacific-East Asian teleconnection pattern in the lower troposphere (Zhang et al. 1999; Wang et al. 2000; Zhang and Sumi 2002). This linkage was further found to be dependent on the spatial patterns of ENSO (Ashok et al. 2007; Weng et al. 2009; Feng et al. 2010). In addition, Nan and Zhao (2012) reported that pre-existing thermal conditions over the Asian continent play a role just as important as ENSO in the interannual variability of extreme precipitation events over South China.

The characteristic time scale of a wintertime precipitation event falls within the synoptic timescale ranging from several hours to several days. Consequently, to gain a deeper understanding of the dynamics of the wintertime precipitation over South China, it is necessary and natural to study it from a synoptic perspective. However, few of these previous studies examined the wintertime precipitation over South China from the synoptic perspective. For those studies that did adopt a synoptic perspective, most focused on a single precipitation event (Zhou et al. 2009; Hong and Li 2009; Wen et al. 2009; Bueh et al. 2011), particularly the severe snow storm event during January 2008, or several precipitation events during the winter of a single year (Yao and Huang 2016). The few studies (Zong et al. 2014; Lou et al. 2017; Ding and Li 2017) that identified the synoptic circulation patterns responsible for the occurrence of persistent heavy precipitation events considered only events with durations exceeding two days. However, during most winters, the number of heavy precipitation events with lifetimes exceeding two days is small. For example, Zong et al. (2014), Lou et al. (2017), and Ding and Li (2017), using different criteria defining a heavy precipitation event, identified only 21, 27 and 30 persistent heavy precipitation events in 32, 57, and 65 winters, respectively. For the persistent events that

were identified, all of these studies pointed out that a Rossby wave train originating from the North Atlantic Ocean and surrounding continental areas and propagating across the Mediterranean and Arabian Seas and into East Asia, plays an essential role in generating circulation patterns conducive to persistent heavy precipitation events. Therefore, the occurrence frequency of persistent heavy precipitation events during winter ranges from 0.46 to 0.66 per year depending on the definition of a heavy precipitation event. This suggests that only a small fraction of extreme precipitation events can be directly explained by the proposed Rossby wave train mechanism. One question that arises is whether the proposed Rossby wave mechanism for persistent heavy precipitation events applies to the extreme precipitation events with shorter lifetimes that are more common in South China. Further, in addition to the mechanisms initializing the circulation patterns associated with extreme precipitation events over South China, are there any local pre-conditions over South China necessary for the development of extreme precipitation events? These questions have not been addressed from the synoptic perspective by any of these previous studies.

This study is designed to explore the mechanism responsible for the occurrence of extreme precipitation events regardless of their durations and identify any critical local pre-conditions necessary for their development. This paper is organized as follows: Sect. 2 describes the precipitation and reanalysis datasets and the methodology used in this study. Section 3 briefly introduces the basic characteristics of the identified extreme precipitation events over South China. Section 4 classifies the extreme precipitation events into two types depending upon the presence or absence of the European blocking high precursor. Approximately 77% of extreme precipitation events over South China are preceded by European blocking events. Section 5 examines the time evolution of circulation and temperature anomalies associated with precipitation events with pre-existing European blocking highs. Section 6 examines the moisture budget for precipitation events with pre-existing European blocking highs. A summary and concluding remarks are provided in Sect. 7.

2 Data and methods

2.1 Data

This study focuses on the extreme precipitation events over South China (105–123°E, 20–32°N) that occurred during the winter months from 1979 to 2013. In this study, the winter of a specific year refers to December of that year, and January and February (DJF) of the following year. In

total, the analysis period includes 3159 winter days between December 1979 and February 2014.

The observational precipitation data used herein is from China Meteorological Administration (http://data.cma.cn/data/cdcdetail/dataCode/SURF_CLI_CHN_MUL_DAY_V3.0.html), which is constructed from observations taken at the 2474 surface meteorological stations in China. To avoid missing data bias in the analysis, stations having any missing value during DJF 1979–2013 are excluded. In total, there are 2252 surface stations over continental China without any missing values (Fig. 1a). Specifically, the number of surface stations without any missing values over South China is 770, which is much denser than that in the western and northeastern parts of China. The relatively dense station coverage in South China suggests that station-based data in this area may have a high utility for recognizing and characterizing precipitation events. The observed long-term average precipitation during the DJF 1979–2013 time period had its maximum in South China, with the average precipitation at most stations exceeding 2 mm day^{-1}. The overall station-based average precipitation over South China during DJF 1979–2013 was 1.70 mm day^{-1}.

In addition to the precipitation data, atmospheric state data is taken from the National Centers for Environmental Prediction and the National Center for Atmospheric Research reanalysis (NCEP-NCAR; Kalnay et al. 1996). This data includes the daily geopotential height, winds, air temperature, and specific humidity on 17 pressure levels extending from 1000 to 10 hPa, sea level pressure, surface pressure, near-surface air temperature and specific humidity at 2 m height, precipitable water content, and surface downward long wave radiation, latent and sensible heat fluxes.

If not explicitly noted, the daily anomalies for a variable throughout this study are estimated with respect to the composite average of that variable for each calendar day during DJF 1979–2013.

2.2 Identification of wintertime extreme precipitation events over South China

The extreme precipitation events over South China are identified using the following procedure. First, for each winter day, the station-based average precipitation for South China is estimated as the average precipitation over all 770 stations. Second, an extreme precipitation day is identified when the station-based average precipitation exceeds the 90th percentile (4.86 mm day^{-1}) of all daily station-based average precipitation. Using this criterion, there are a total of 316 days identified as having extreme precipitation. Third, any time period with consecutive extreme precipitation days is

Fig. 1 Horizontal distributions of the composite average precipitation (units: mm day^{-1}) over the continental areas of China during **a** DJF 1979–2013 and **b** 316 extreme precipitation days. Note that only the stations without any missing values are plotted. Distributions in the number of extreme precipitation events versus **c** their lifetimes (units: days) and **d** station-based average precipitation (units: mm day^{-1}) over South China. **e** The time evolution of the annual number of extreme precipitation events and their associated annually-accumulated durations (units: days)
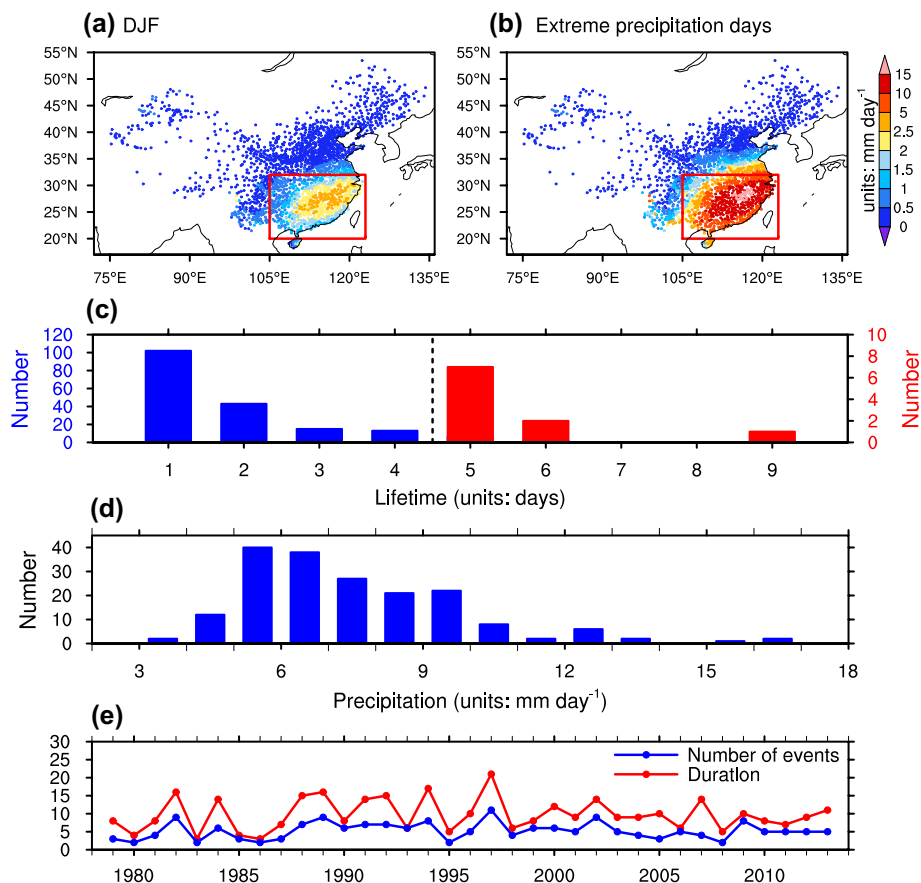
recognized as an extreme precipitation event. In addition, the definition also allows for an extreme precipitation event to have one non-extreme precipitation day between two extreme precipitation days. Based on this algorithm, there were 183 extreme precipitation events detected during the DJF 1979–2013 time period.

2.3 Wave activity flux

The wave activity flux is a useful diagnostic tool for examining the energy dispersion characteristics associated with a Rossby wave train (Plumb 1985; Takaya and Nakamura 2001; Wu et al. 2003; Tam and Li 2006). We use the horizontal formulation of the wave activity flux $\mathbf{W}_{2d}$ from Plumb (1985), which is computed as:

$$\mathbf{W_{2d}} = \frac{p}{p_0} \cos\phi \begin{pmatrix} \frac{1}{2a^2 \cos^2\phi} [(\frac{\partial\psi'}{\partial\lambda})^2 - \psi'\frac{\partial^2\psi'}{\partial\lambda^2}] \\ \frac{1}{2a^2 \cos\phi} [\frac{\partial\psi'}{\partial\lambda}\frac{\partial\psi'}{\partial\phi} - \psi'\frac{\partial^2\psi'}{\partial\lambda\partial\phi}] \end{pmatrix}, \quad (1)$$

where (λ, ϕ) are the longitude and latitude, p is the pressure, p_0 is the reference pressure ($p_0 = 1000$ hPa), a is the radius of Earth, and (ψ, ψ') are the geostrophic streamfunction and its deviation with respect to the zonal mean.

3 Basic characteristics of extreme precipitation events

Figure 1b shows the distribution of the composite precipitation for the 2252 surface stations without missing values for the 316 extreme precipitation days identified by the algorithm given in Sect. 2.2. The average precipitation for the majority of the 770 surface stations in South China exceeded 10 mm day^{-1}, while the overall average station-based precipitation in South China was 8.16 mm day^{-1}. Further, during these extreme precipitation days, there were 27 stations in South China with average precipitation exceeding 15 mm day^{-1}.

We have estimated the lifetimes for the 183 extreme precipitation events, which were comprised primarily of the 316 extreme precipitation days plus the few non-extreme precipitation days that fall within a sequence of extreme precipitation days and get included by the selection algorithm. The lifetimes of extreme precipitation events ranged from one to nine days (Fig. 1c). The distribution being 102 events with lifetimes of one day (55.7% of the total), 43 events with lifetimes of two days (23.5%), 28 events with lifetimes that ranged from three to four days (15.3%), and 10 events with lifetimes that ranged from 5 to 9 days (5.5%). The station-based average precipitation of these events ranged from 3.58 to 16.71 mm day^{-1} (Fig. 1d), with 14 events having

precipitation of less than 5 mm day^{-1}, 148 events with precipitation that ranged from 5 to 10 mm day^{-1}, and 21 events with precipitation that exceeded 10 mm day^{-1}.

Noticeable interannual variability can be observed in the annual number of extreme precipitation events and the associated annually-accumulated durations for each winter during the study period (Fig. 1e). The annual number of extreme precipitation events ranged from 2 to 11, while the associated annually-accumulated duration ranged from 3 days to 21 days. The overall average of the annual number of the extreme precipitation events was 5.23 with a standard deviation of 2.31, while the overall average of the annually-accumulated duration of these events was 9.74 days with a standard deviation of 4.43 days.

4 A two-type classification of extreme precipitation events

4.1 Synoptic circulation patterns during extreme precipitation events

To identify the circulation patterns favorable to the 183 extreme precipitation events over South China, the composite geopotential height anomalies at four different pressure levels (100, 300, 500, and 850 hPa) during the days belonging to these events are presented in Fig. 2a–d. On nearly all the four levels, significant anticyclonic and cyclonic anomalies can be observed over the region extending from the Arabian Sea eastward to the west coast of North America. The anomaly amplitudes were the largest on the 300 hPa surface (Fig. 2b) and there were seven centers of action on this surface; three anticyclonic anomalies centered at (70°E, 22.5°N), (132.5°E, 37.5°N), and (165°W, 50°N), and four cyclonic anomalies centered at (77.5°E, 42.5°N), (105°E, 30°N), (165°E, 35°N), and (125°W, 47.5°N). Significant anticyclonic and cyclonic anomalies of smaller magnitude can also be observed near these seven centers on the other three pressure surfaces, indicating that the associated circulation pattern tends to be a barotropic response.

To depict the vertical structure of the associated circulation patterns, we composite the geopotential height anomalies on a vertical cross section that moves along with the seven centers of action on the 300 hPa level for all extreme precipitation events. Note that 17 isobaric surfaces (1000, 925, 850, 700, 600, 500, 400, 300, 250, 200, 150, 100, 70, 50, 30, 20, and 10 hPa) are used to estimate the vertical distribution. As shown in Fig. 2e, the extreme values of the geopotential height anomalies were all located near the 300 hPa surface. Specifically, all seven anomaly centers extended over nearly the entire troposphere (ranging from 100 to 1000 hPa; although they were not significant on some

Fig. 2 Distributions of the composite geopotential height anomalies (contour and shading; units: gpm) during all the 183 extreme precipitation events. **a–d** The composite geopotential height anomalies on the 100, 300, 500, and 850 hPa surfaces, respectively. The green line with seven points denotes six great circle arcs between the seven centers of action in the geopotential height anomalies on the 300 hPa surface. **e** The vertical cross section of composite mean of geopotential height anomalies (units: gpm) along the green line. Shading indicates that the composite value meets the 95% confidence level based on two-tailed Student's t tests
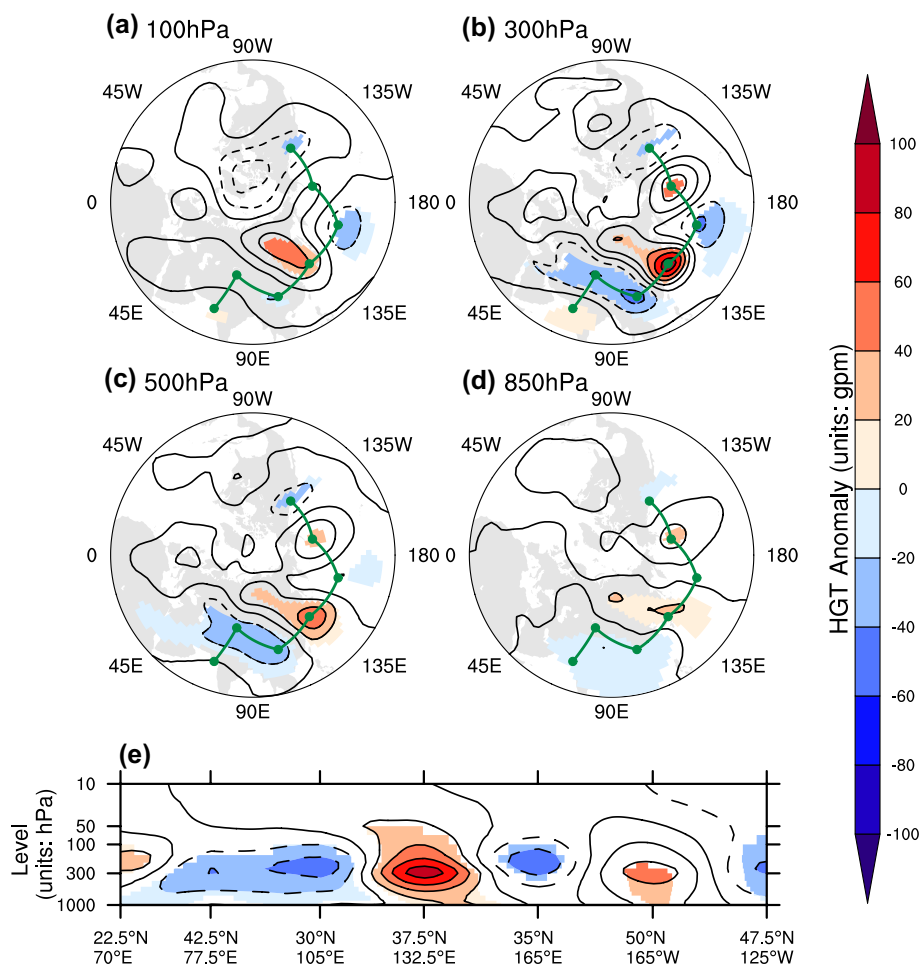
surfaces), further confirming the barotropic characteristic of the circulation pattern. Further, significant cyclonic anomalies spanned from the Caspian Sea to South China. Note that, the cyclonic anomalies in the lower troposphere (850 hPa) covered more area of South China than those in the middle and upper troposphere. On one hand, these cyclonic anomalies were conducive to updrafts that would lead to precipitation over South China. On the other hand, these cyclonic anomalies also corresponded to weakened northerly winds along the coastal areas of East Asia and surrounding oceans, which was conducive to the transport of water vapor from the surrounding oceans into South China. The role of these cyclonic anomalies on the updraft and water vapor transport will be analyzed in Sects. 5.1 and 6.

4.2 Time evolution of the circulation patterns for extreme precipitation events

To understand the triggering mechanism for wintertime extreme precipitation events over South China, it is necessary to understand the formation mechanisms for the circulation patterns favorable to extreme precipitation

events. This subsection uses composite analysis on the 300 hPa surface to identify precursor signals favorable to the development of circulation patterns leading to extreme precipitation events. The composite analysis is conducted as follows: First, the time evolution of physical variables for each extreme precipitation event are formulated as $X = X(i, j, n)$, where (i, j) are the grid point indices along the zonal and meridional directions, respectively, and n is the index for the day relative to the onset of the extreme precipitation event. Second, we compute a temporal composite of the 183 extreme precipitation events, so that the composite distribution of X on day n is the average of X for all extreme precipitation events on day n.

Figure 3 illustrates the time evolution of the horizontal distribution of the composite geopotential height anomalies on the 300 hPa surface from day − 12 to day + 4 at an interval of 2 days. At the onset of precipitation events (day 0; Fig. 3g), the circulation pattern was similar to that during the periods of all the events (Fig. 2b). Specifically, on day 0, there were cyclonic anomalies that spanned from the area east of the Caspian Sea to South China (Fig. 3g) with a center located over South China.

Fig. 3 Time evolution of the composite geopotential height anomalies (contour and shading; units: gpm) on the 300 hPa surface from day − 12 to day + 4 (with an interval of 2 days) for all the 183 extreme precipitation events. Shading indicates that the composite value meets the 95% confidence level based on two-tailed Student's *t* tests
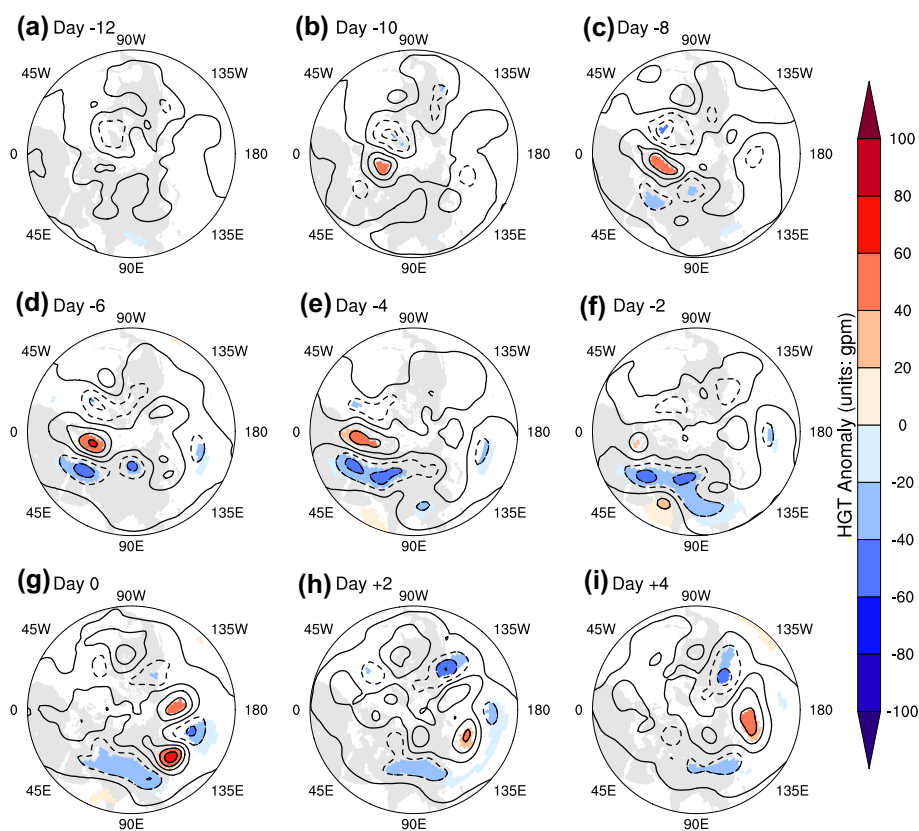
About 10 days prior to the onset of extreme precipitation, an anticyclonic anomaly formed over Western Europe (Fig. 3b; day − 10). This anticyclonic anomaly lasted from day − 10 to around day − 2 (Fig. 3b–f), giving it an estimated lifetime of ∼ 9 days. Since no significant movement in the center of the anticyclonic anomaly was observed over its lifetime, this anomaly can be viewed as a quasi-stationary blocking high over Europe (Barriopedro et al. 2006; Diao et al. 2006; Woollings et al. 2008; Cheung et al. 2012; Davini et al. 2012, 2014). On day − 8, two cyclonic anomalies formed downstream of the European anticyclonic anomaly (Fig. 3c). Six days after the formation of the European anticyclonic blocking anomaly, a Rossby wave-like train had formed consisting of the persistent European anticyclonic anomaly, two cyclonic anomalies downstream of the European anticyclonic anomaly, an anticyclonic anomaly over the Arabian Sea, and a cyclonic anomaly over East Asia (Fig. 3e–f; day − 4 and − 2). As the onset of the extreme precipitation events approached, the cyclonic anomaly over East Asia slowly moved towards South China (Fig. 3e–g), significantly intensifying the cyclonic anomaly over South China.

4.3 A two-type classification based on the pre-existing European blocking

Since persistent, quasi-stationary, anticyclonic anomalies were present over Western Europe prior to the onset of extreme precipitation events, the European blocking events may play a dominant role in the formation of favorable circulation patterns necessary for the development of extreme precipitation events over South China during winter. Therefore, it is important to determine whether every extreme precipitation event over South China was preceded by a European blocking event.

In this subsection, the 183 identified extreme precipitation events are classified into two different types depending on whether or not a European blocking circulation pattern existed any time from day − 10 to the onset of the extreme precipitation event. The atmospheric blocking event tracking algorithm developed by Barriopedro et al. (2006) is used to judge whether the circulation pattern for a specific day is associated with European blocking. This algorithm includes the following three steps: First, identify

all blocked longitudes within 5°W–45°E by calculating the following three indices:

$$
\begin{cases}
\text{GHGS} = \dfrac{Z(\lambda,\phi_0)-Z(\lambda,\phi_S)}{\phi_0-\phi_S} \\[2mm]
\text{GHGN} = \dfrac{Z(\lambda,\phi_N)-Z(\lambda,\phi_0)}{\phi_N-\phi_0} \\[2mm]
Z_{\text{ano}} = Z(\lambda,\phi_0) - \overline{Z(\lambda,\phi_0)}
\end{cases}
, \qquad (2)
$$

where $Z(\lambda,\phi)$ is the daily geopotential height at 300 hPa for the grid cell centered at longitude λ and latitude ϕ, GHGS and GHGN represent the meridional gradients of the geopotential height over the southern and northern latitudes, respectively and Z_{ano} is the daily geopotential height anomaly with respect to the average over all the days with the same calendar date. Note that when applying the algorithm, the geopotential height must be on a uniform longitude-latitude grid with a resolution of 2.5°. Also note that although the original algorithm was applied to the geopotential height at 500 hPa, a change to 300 hPa was done for this study to be consistent with the pressure level used in the composite analysis in Sects. 4.1 and 4.2. The ϕ_S, ϕ_0, and ϕ_N have the following values:

$$
\begin{cases}
\phi_S = 40.0°\text{N} + \Delta \\
\phi_0 = 60.0°\text{N} + \Delta \\
\phi_N = 77.5°\text{N} + \Delta \\
\Delta = -5.0°, -2.5°, 0, 2.5°, 5.0°
\end{cases}
, \qquad (3)
$$

where the five different values of Δ correspond to five different sets of the three indices in Eq. (2). A longitude is defined as 'blocked' when the three indices in Eq. (2) meet the following conditions for at least one of the five Δ:

$$
\begin{cases}
\text{GHGS} > 0 \\
\text{GHGN} < -10 \text{ gpm}(°\text{lat})^{-1} \\
Z_{\text{ano}} > 0
\end{cases}
. \qquad (4)
$$

Second, a day is considered 'associated with European blocking' when at least five consecutive longitudes (12.5°) within the region (5°W–45°E) are determined to be blocked. Third, an extreme precipitation event is regarded as 'associated with European blocking' when there is at least one day identified as possessing European blocking during the period between day −10 to day −1. We do not take into account the persistence of the blocking event, due primarily to the possibility that atmospheric blocking may originate from the upstream of the region under analysis (5°W–45°E) and/or initialize before day −10.

After applying this algorithm, the number of the extreme precipitation events determined to be associated with and without European blocking are 141 and 42, accounting for 77.0% and 23.0% of the precipitation events, respectively. Hereafter, the two types of precipitation events are referred
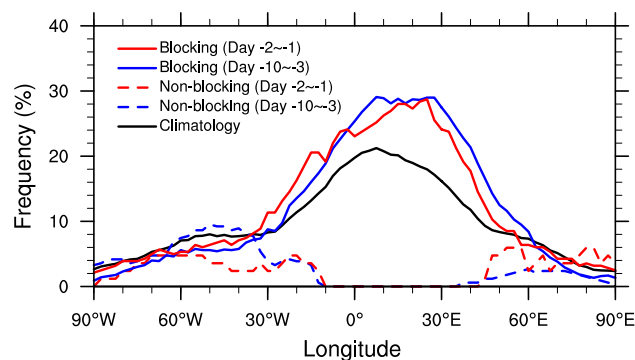

Fig. 4 Longitudinal distribution of blocking frequency at 300 hPa during DJF 1979–2013 and different phases of the two types of extreme precipitation events

to as blocking precipitation events and non-blocking precipitation events. The above algorithm has been applied to calculate the blocking frequency for the entire Northern Hemisphere. Figure 4 displays the longitudinal distribution of the blocking frequency at 300 hPa for wintertime climatology and different phases prior to the onset of both types of extreme precipitation event. The average of the wintertime blocking frequency over Western Europe (5°W–45°E) during DJF 1979–2013 was 17.2%. For non-blocking precipitation events, the average blocking frequency over Western Europe dropped to 0.1% during both the − 10 to − 3 day time period and the − 2 to − 1 day time period. For the blocking precipitation events, the average blocking frequency over Western Europe increased to 25.8% during the − 10 to − 3 day time period and 23.6% during the − 2 to − 1 day time period. These results are consistent with the longitudinal distribution of blocking frequency at 500 hPa (Fig. S1 in Supplementary Material). The horizontal distributions of the precipitation for the two types of precipitation events are shown in Fig. S2. The average precipitation for the blocking type events (7.78 mm day^{-1}) was slightly larger than that for the non-blocking type events (7.63 mm day^{-1}), but the difference was not statistically significant.

As most (77%) of the wintertime extreme precipitation events over South China were preceded by European blocking events, we focus mainly on the formation mechanism for the blocking precipitation events.

5 Circulation and temperature anomalies associated with blocking precipitation events

5.1 Time evolution of circulation patterns

Figure 5 displays the time evolution of the composite geopotential height anomalies and horizontal wave activity

Fig. 5 Time evolution of the composite geopotential height anomalies (contour and shading; units: gpm) and horizontal wave activity fluxes (vector; units: m² s⁻²) on the 300 hPa surface from day − 12 to day + 4 (with an interval of 2 days) for the 141 extreme precipitation events with pre-existing European blocking highs. Shading indicates that the composite geopotential height anomaly meets the 95% confidence level based on two-tailed Student's t tests. Vector is plotted if wave activity fluxes are significant in at least one direction (zonal or meridional)
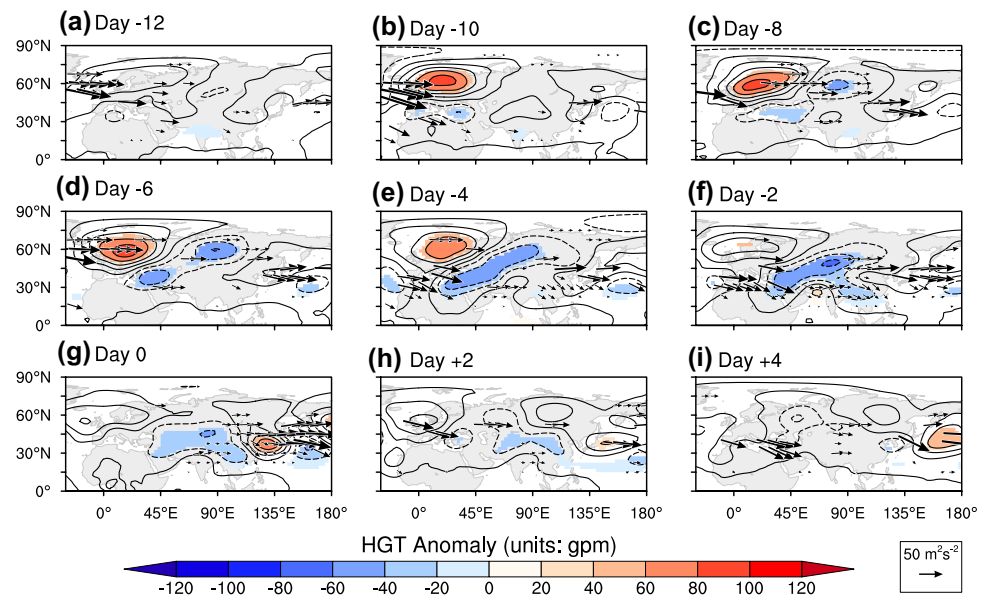
fluxes on the 300 hPa pressure surface for the 141 blocking precipitation events. Similar to the time evolution of the composite geopotential height anomalies for all extreme precipitation events (Fig. 3), the European blocking-related anticyclonic anomalies for the blocking type events also lasted from day − 10 to day − 2 (Fig. 5b–f). Compared to the composite for all precipitation events (Fig. 3b–f), the anticyclonic anomalies for the blocking type events were more intense and of larger horizontal scale. The presence of the European blocking provided continuous wave activity fluxes, which effectively triggered and strengthened the downstream cyclonic anomalies from day − 8 to day − 2 (Fig. 5c–f). One of these cyclonic anomalies, which evolved from a cyclonic anomaly over the Mediterranean Sea on day − 10 (Fig. 5b), was located over the Caspian Sea (near 45°E) on day − 8 (Fig. 5c), while the other cyclonic anomaly formed directly over Central Siberia (70°–90°E) on day − 8 (Fig. 5c).

On day − 2, when the European blocking had significantly weakened, the above two cyclonic anomalies propagated slightly eastward and merged with the cyclonic anomaly over East Asia (Fig. 5f) that appeared on day − 4 (Fig. 5e). In particular, the decay of the European blocking was conducive to the recovery of the powerful westerly winds (Tyrlis and Hoskins 2008), which were favorable to the eastward propagation of cyclonic anomalies. As a consequence, the spatial extent of cyclonic anomalies over East Asia expanded remarkably. On day − 2, together with anticyclonic anomalies located over the Arabian Sea and Western Europe, these cyclonic anomalies constituted a Rossby-like wave train similar to the circumglobal teleconnection pattern over the Eurasian sector during winter (cf. Fig. 3a of Hu et al. 2017). The possible relationship to the circumglobal teleconnection pattern is analyzed further in Sect. 5.2. However, it should

be noted that the anticyclonic anomaly over the Arabian Sea was relatively weak and only observed on day − 2 (Fig. 5f), suggesting its transport of wave activity to the cyclonic anomaly over South China was weak. Therefore, the eastward propagation of the cyclonic anomalies downstream of the European anticyclonic anomaly played an essential role in the formation of the cyclonic anomaly over South China.

By day 0, the cyclonic anomalies to the west of 45°E had disappeared (Fig. 5g), while the majority of South China was covered by the cyclonic anomalies. Meanwhile, to the northeast of East Asia there were significant anticyclonic anomalies, which were triggered by the downstream wave activity flux from the cyclonic anomalies. This East Asian circulation pattern led to southerly wind anomalies over the coastal areas of East Asia, which were conducive to the transportation of water vapor from the coastal ocean to South China. By days + 2 and + 4 (Fig. 5h, i), both the cyclonic anomaly over South China and the downstream anticyclonic anomaly had weakened remarkably relative to day 0, indicating that the extreme precipitation event was approaching its end.

In addition to the horizontal circulation, the vertical motion is also analyzed to further investigate the role of the favorable circulation pattern on extreme precipitation events over South China. Figure 6 shows the time evolution of the vertical cross section of the meridionally-averaged relative vorticity anomalies and wind anomalies within 20–32°N for the blocking type events. By day − 8, there were significant positive relative vorticity anomalies and anomalous ascending motions around 100–110°E, but they were relatively weak and confined to the lower troposphere (1000–850 hPa; Fig. 6c). As the East Asian cyclonic anomaly initialized on day − 4 (Fig. 5e), significant positive relative vorticity anomalies appeared in the middle and upper troposphere (500–300 hPa) around 90°E. Due to the
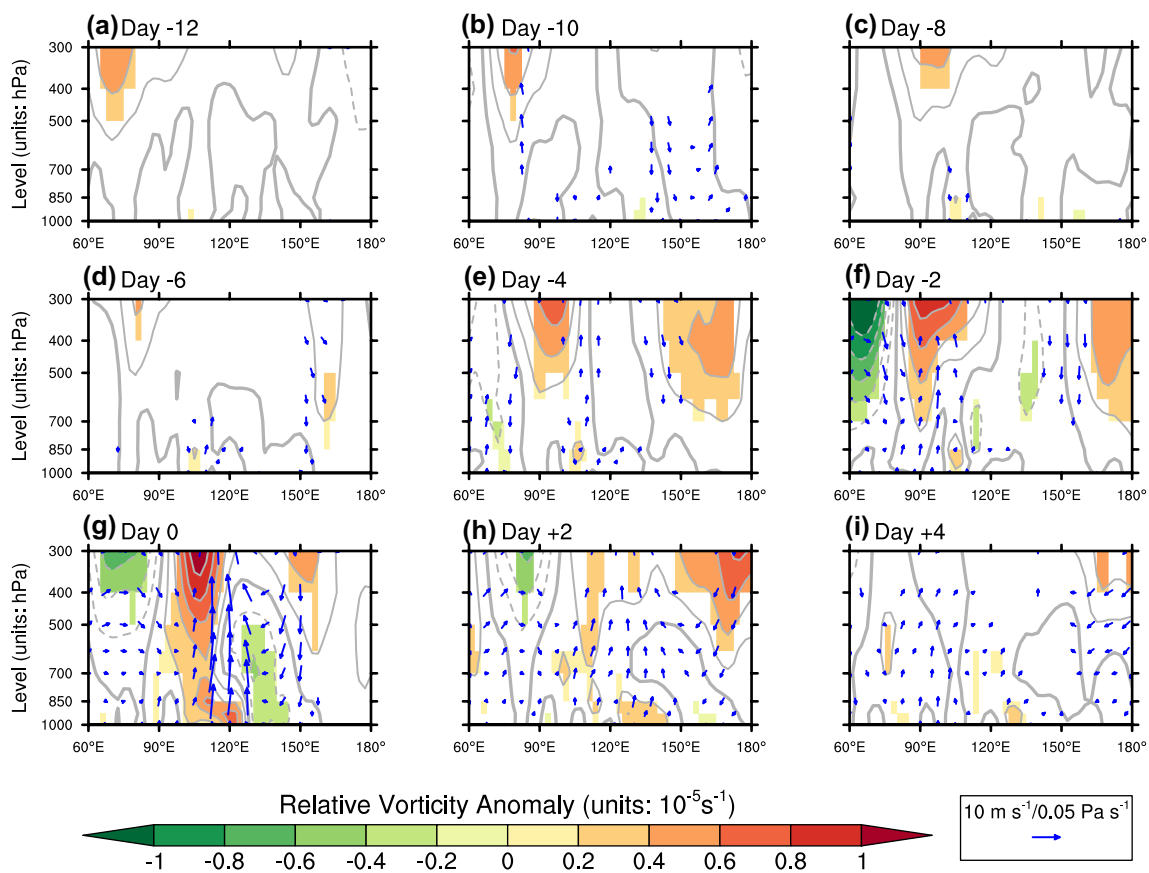
Fig. 6 Time evolution of the vertical cross section of the meridionally-averaged composite relative vorticity anomalies (contour and shading; units: 10^{-5} s^{-1}) and wind anomalies (zonal and vertical components; vector; units: zonal in m s^{-1}, vertical in Pa s^{-1}) over the South China region within 20–32°N from day − 12 to day + 4 (with an interval of 2 days) for the 141 extreme precipitation events with pre-existing European blocking highs. The sign of vertical velocity ($\frac{dp}{dt}$) is reversed to make the ascending motions in the upward direction. Shading and vector indicate that the composite values meet the 95% confidence level based on two-tailed Student's t tests. Vector is plotted if wind anomalies are significant in at least one direction (zonal or vertical)

eastward propagation of these cyclonic anomalies (Fig. 5f), the positive relative vorticity anomalies over East Asia were significantly enhanced and occupied nearly the entire troposphere (Fig. 6f) and enhanced anomalous ascending motions can be observed. At the onset of the extreme precipitation event, the positive relative vorticity anomaly and the anomalous ascending motion reached their maximum intensity (Fig. 6g). These anomalous ascending motions were conducive to the lifting and condensation of water vapor and feed the enhanced precipitation over South China. As the extreme precipitation event approached its end, both the positive relative vorticity and ascending motion anomalies weakened dramatically relative to their levels on day 0 (Fig. 6g–i).

5.2 Possible relationship to the circumglobal teleconnection pattern

As mentioned in Sect. 5.1, the circumglobal teleconnection pattern may play a role in the formation of blocking-type

precipitation events. Following Branstator (2002), based on the empirical orthogonal function (EOF) analysis technique, the circumglobal teleconnection pattern over the Eurasian sector is obtained as the leading mode of monthly-mean nondivergent meridional wind anomalies at 300 hPa in the region 0–120°E, 0–45°N during DJF 1979–2013. As discussed by Branstator (2002), the nondivergent meridional wind is chosen in lieu of geopotential height or streamfunction because this variable has no zonal mean and thus emphasizes circulation anomalies with shorter zonal scales trapped in the jet stream. The leading mode can explain 28.2% of the total variance. Figure 7a shows the spatial distribution of nondivergent meridional wind anomalies during the winter months of 1979–2013 regressed against the normalized PC1, which can be viewed as the spatial expression of the circumglobal teleconnection. The circumglobal teleconnection pattern is a zonally-oriented wave train characterized by alternating centers of northerlies and southerlies extending from Western Europe to East Asia. This wave
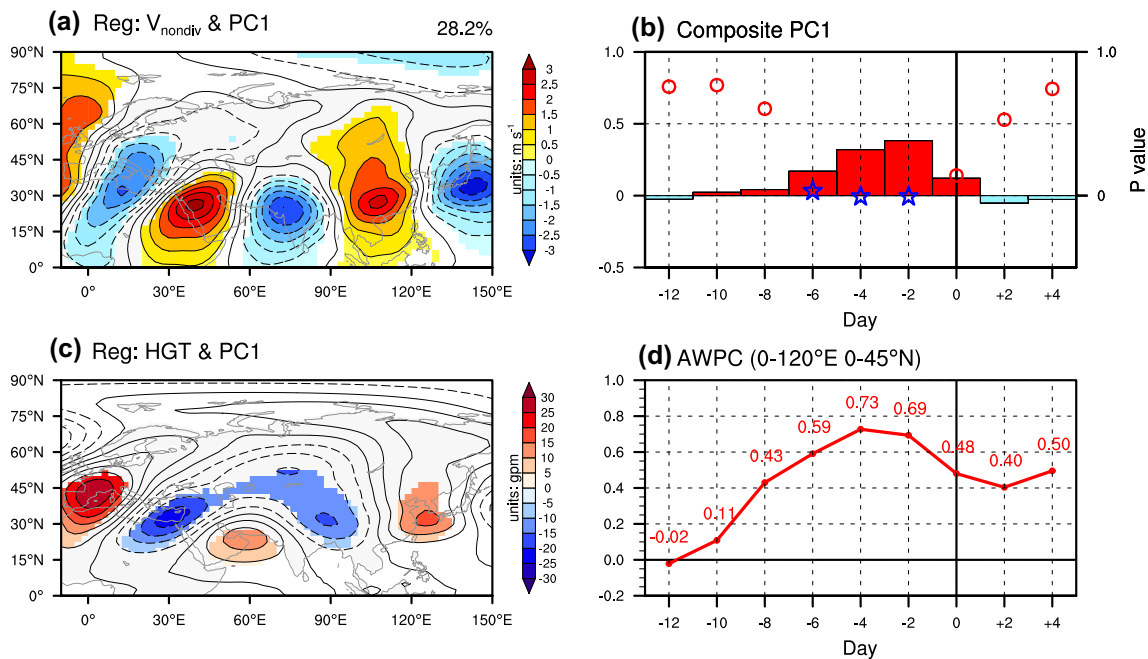
Fig. 7 Spatial distributions of monthly **a** nondivergent meridional wind anomalies (contour and shading; units: m s⁻¹) and **c** geopotential height anomalies (contour and shading; units: gpm) on the 300 hPa surface regressed onto the normalized PC1 of monthly nondivergent meridional wind anomalies at 300 hPa in the 0–120°E, 0–45°N domain during DJF 1979–2013. The explained variance is shown in the top right corner of panel **a**. Shading indicates that the regression is significant at the 95% confidence level based on a two-tailed Student's *t* test. **b** Composite evolution of the normalized PC1 (bar) for the 141 extreme precipitation events preceded by European blocking highs. The *P*-value of the composite index for each day is estimated using a two-tailed Student's *t* test. *P*-values smaller than 0.05 are denoted by blue stars; those larger than 0.05 are denoted by red circles. **d** Time evolution of area-weighted pattern correlations (AWPCs) between the composite geopotential height anomalies over the region of 0–120°E, 0–45°N for the blocking precipitation events and the regression maps of the geopotential height against the normalized PC1 from day − 12 to day + 4 (with an interval of 2 days)

train is essentially an eastward-propagating Rossby wave packet traveling within the local time-mean jet core (Feldstein and Dayan 2008). The trapping effect of the jet stream on anomalies in the wave train inhibits meridional dispersion and enables the circumglobal teleconnection pattern to span nearly all longitudes in the Northern Hemisphere. A daily index for the circumglobal teleconnection pattern is obtained by projecting daily nondivergent meridional wind anomalies onto the spatial pattern of the leading mode. This daily index is normalized to have a mean of zero and a standard deviation of one over DJF 1979–2013.

Figure 7b shows the composite time evolution of the circumglobal teleconnection pattern index for the Eurasian sector before and during blocking-type precipitation events. The period from day − 6 to day − 2 before blocking-type precipitation events was characterized by significant positive indices, with a peak value on day − 2 (Fig. 7b), coincident with the formation of a Rossby-like wave train over the Eurasian continent (Fig. 5f). Southerly wind anomalies prevailed at 300 hPa over South China under the positive phase of the circumglobal teleconnection pattern (Fig. 7a). Southerly wind anomalies were also evident in the lower troposphere over South China at this time (Fig.

S3 in supplementary material), favoring enhanced moisture transport from the south. Figure 7c shows 300-hPa geopotential height anomalies regressed onto the normalized PC1 during the winter months of 1979–2013. The positive phase of the circumglobal teleconnection pattern was characterized by anticyclonic anomalies over Western Europe and the Arabian Sea and cyclonic anomalies over the Mediterranean Sea and western parts of East Asia. This structure evoked the composite circulation pattern on day − 2 (Fig. 5f). Figure 7d shows the evolution of area-weighted pattern correlations (AWPC) between composite geopotential height anomalies within 0–120°E, 0–45°N and geopotential height anomalies regressed onto the normalized PC1 before and during blocking-type extreme precipitation events. The AWPCs ranged from 0.59 to 0.73 for the days with significant positive composite PC1 indices (days − 6 through − 2; Fig. 7b), further confirming the similarity between the circumglobal teleconnection pattern and circulation pattern that favored blocking-type extreme precipitation events over South China. We therefore argue that blocking-type precipitation events over South China were closely related to the positive phase of the circumglobal teleconnection pattern in the Eurasian sector.

5.3 Time evolution of temperature anomalies

The time evolution of surface temperature and sea level pressure anomalies during blocking-type extreme precipitation events is shown in Fig. 8. In the blocking type precipitation events, from day − 10 to day − 4, significant surface anticyclonic anomalies were present over Western Europe, suggesting the barotropic characteristic of the Western European blocking (Fig. 8b–e). Upstream of these surface anticyclonic anomalies, there were southerly winds associated with warm advection. As a consequence, there were significant warm surface temperature anomalies over the Scandinavian Peninsula from day − 10 to day − 4. Downstream of these surface anticyclonic anomalies, there were northerly winds associated with cold advection. Therefore, there were significant cold surface temperature anomalies to the west of Caspian Sea from day − 8 to day 0 (Fig. 8c–g).

In the blocking type precipitation events, there were weak, but significant negative sea level pressure anomalies downstream of the anticyclonic anomalies over Western Europe from day −8 to day − 6 (Fig. 8c, d), indicating an inhibition of the Siberian High during this period (black line in Fig. 9). Note that herein the intensity of Siberian High is defined as the area-averaged sea level pressure anomaly within the domain 80–120°E, 40–60°N (Wu and Wang 2002). As a consequence, significant and well-organized warm temperature anomalies existed over South China during the period
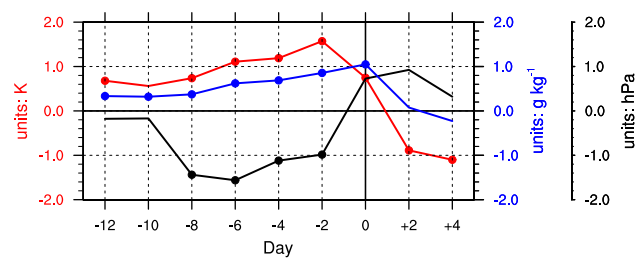

Fig. 9 Time evolution of area-averaged composite surface temperature anomalies (units: K; red line) and specific humidity anomalies at 2 m height (units: g kg^{-1}; blue line) over the land areas of South China (105–123°E, 20–32°N), and composite Siberian High index anomalies (units: hPa; black line) from day − 12 to day + 4 (with an interval of 2 days) for the 141 extreme precipitation events with pre-existing European blocking highs

from day − 6 to day − 2 (Fig. 8d–f). According to the Clausius-Clapeyron relationship (Trenberth et al. 2003; Held and Soden 2006; O'Gorman and Muller 2010), the pre-existence of warm anomalies led to the formation of positive specific humidity anomalies in the lower troposphere over South China (blue line in Fig. 9). However, these negative sea level pressure anomalies disappeared by day − 4 (Fig. 8e). On day − 2, significant surface cyclonic anomalies were present to the southwest of Lake Baikal (Fig. 8f), which was the surface signature of the eastward movement of the upper tropospheric cyclonic anomaly (Fig. 5f).
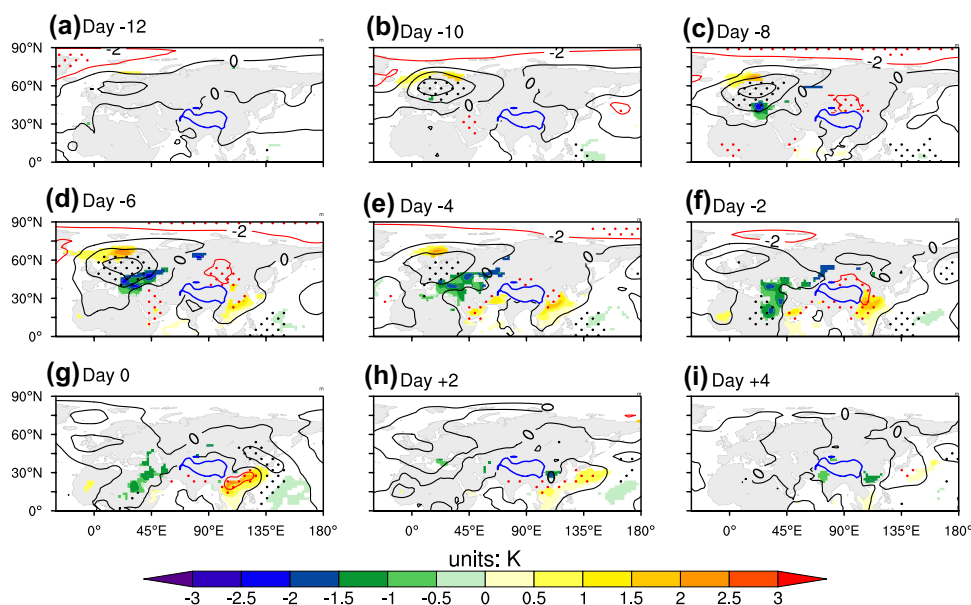

Fig. 8 Time evolution of the composite surface temperature anomalies (shading; units: K) and sea level pressure anomalies (contour with an interval of 2 hPa; units: hPa) from day − 12 to day + 4 (with an interval of 2 days) for the 141 extreme precipitation events with pre-existing European blocking highs. Only the surface temperature anomalies that meet the 95% confidence level based on two-tailed Student's *t* tests are plotted. Negative (positive and zero) contours are shown by red (black) lines. Red (black) dotted areas indicate that the negative (positive and zero) composite sea level pressure anomalies meet the 95% confidence level based on two-tailed Student's *t* tests. Regions bounded by blue lines have surface altitudes exceeding 2500 m

At the onset of the blocking type precipitation events, significant surface cyclonic anomalies moved into South China and overlapped with the pre-existing warm temperature anomalies (Fig. 8g). Moreover, the sea level pressure anomalies to the north of South China were significantly enhanced, which was associated with a southward movement of cold temperature anomalies (not significant; Fig. S4) and rapid intensification of the Siberian High (black line in Fig. 9). On day 0, the scattered cold temperature anomalies over North China and the pre-existing warm temperature anomalies formed a frontal structure. On day +2, the cold temperature anomalies replaced the pre-existing warm temperature anomalies, so that warm temperature anomalies were only present over the adjacent ocean (Fig. 8h). Although the cold anomalies to the north of the pre-existing warm temperature anomalies were relatively weak before the onset of the extreme precipitation event, their collision with the pre-existing warm temperature anomalies played an indispensable role in the formation of the blocking type of precipitation events.

When the blocking type precipitation events appeared over South China, the Siberian High was remarkably enhanced, and a cold surge arrived. Figure S5 in the Supplementary Material displays the composite geopotential height and horizontal wind anomalies on the 850 hPa surface for the blocking extreme precipitation events on days −2, 0, and +1. At day −2, there were no northerly wind anomalies over South China (Fig. S5a). However, the blocking precipitation events possessed easterly wind anomalies that formed around 35°N on day 0, concurrently with significant northerly wind anomalies that formed in the northwestern part of South China (Fig. S5b). By day +1, the northerly component of the wind anomalies over South China was significantly intensified (Fig. S5c). According to Wu and Chan (1995, 1997), the concurrence of increased sea level pressure, reduced surface temperature, and strengthened northerly winds indicated the arrival of the northerly type of monsoon surge, which is usually associated with the passage or formation of a cold front.

A heat budget analysis is conducted to further examine the variations in temperature over land areas of South China. Following Yao et al. (2017), the tendency of surface air temperature includes four components: horizontal temperature advection ($T_{advection}$), adiabatic warming or cooling by vertical motion ($T_{adiabatic}$), the surface downward infrared radiation (IR) flux, and the sensible and latent heat (SLH) fluxes. The first two components ($T_{advection}$ and $T_{adiabatic}$) are estimated on the 850 hPa surface (Yanai et al. 1973; Yanai and Tomita 1998), while the other two components are calculated at the surface. As demonstrated in Sect. 5.1, blocking-type extreme precipitation events were typically triggered by the eastward propagation of cyclonic anomalies into South China prior to day 0. The area downstream of such cyclonic

anomalies was dominated by southerly wind anomalies associated with warm advection. The warmer air introduced by southerly wind anomalies can warm the underlying land surface of South China through downward sensible heat flux. Meanwhile, updrafts associated with the cyclonic anomalies not only led to adiabatic cooling but also favored the formation of deep convective clouds that increased the downward IR flux to the surface. As a consequence, $T_{advection}$, IR, and SLH all contributed to the near-surface temperature increase over South China leading up to the onset of blocking-type extreme precipitation events (day −6 ~day −2; Fig. 10a, c, d). The contribution from $T_{adiabatic}$ tended to reduce air temperature (Fig. 10b). The net effect of the four components was to warm the atmosphere above South China prior to the occurrence of the extreme precipitation. The onset of the extreme precipitation event (day 0) was characterized by a sharp increase in the amplitude of the cooling induced by vertical motion ($T_{adiabatic}$; Fig. 10b), associated with the amplification of the cyclonic anomaly over South China. By contrast, the warming tendency due to horizontal advection ($T_{advection}$) is slightly reduced during and after onset relative to its peak value on day −2 (Fig. 10a), further confirming the existence of cold advection southward into the northern parts of South China.

6 Moisture budget analysis for the blocking precipitation events

Moisture supply plays an essential role in the formation of precipitation events (Li and Zhou 2016; Li et al. 2016). This section is devoted to understanding the moisture budget for the blocking precipitation events. According to Trenberth and Guillemot (1995), the moisture budget equation can be written as:

$$P = -\frac{\partial w}{\partial t} - \nabla \cdot \frac{1}{g} \int_{P_s}^{p_t} q\mathbf{v}dp + E, \tag{5}$$

where P is the precipitation, g is the acceleration of gravity, q is the specific humidity, p is the pressure, p_s is the pressure at surface, p_t is the pressure at 300 hPa, $\mathbf{v}$ is the horizontal wind vector, w is the precipitable water (defined as the mass-weighted vertical integral of the specific humidity: $w = \frac{1}{g} \int_{p_s}^{p_t} qdp$), and E is the moisture evaporation from the surface. The second term on the right-hand side of Eq. (5) represents the contribution to the precipitation by moisture convergence, which is calculated as the sum of the moisture fluxes across the boundaries of South China. These boundaries include the western boundary (red line in Fig. S6), the northern boundary (yellow line in Fig. S6), and the curved southeastern coastal boundary between South China and the

Fig. 10 Time evolution of contributions to the composite surface temperature variations (units: W m^{-2}) from day − 6 to day + 4 (with an interval of 2 days) by four different physical processes for the 141 extreme precipitation events with pre-existing European blocking highs. The four physical processes include **a** horizontal temperature advection ($T_{advection}$), **b** adiabatic warming/cooling by vertical motions ($T_{adiabatic}$), **c** surface downward infrared radiation (IR) flux, and **d** sensible and latent heat (SLH) fluxes. **e** The sum of the contribution by the four different physical processes. In panels **a**–**e**, the composite value with a P value not exceeding 0.05 based on the two-tailed Student's t tests is denoted by a dot. **f** The average contributions of the four different physical processes and their total contribution to surface temperature variations from day − 6 to day − 2
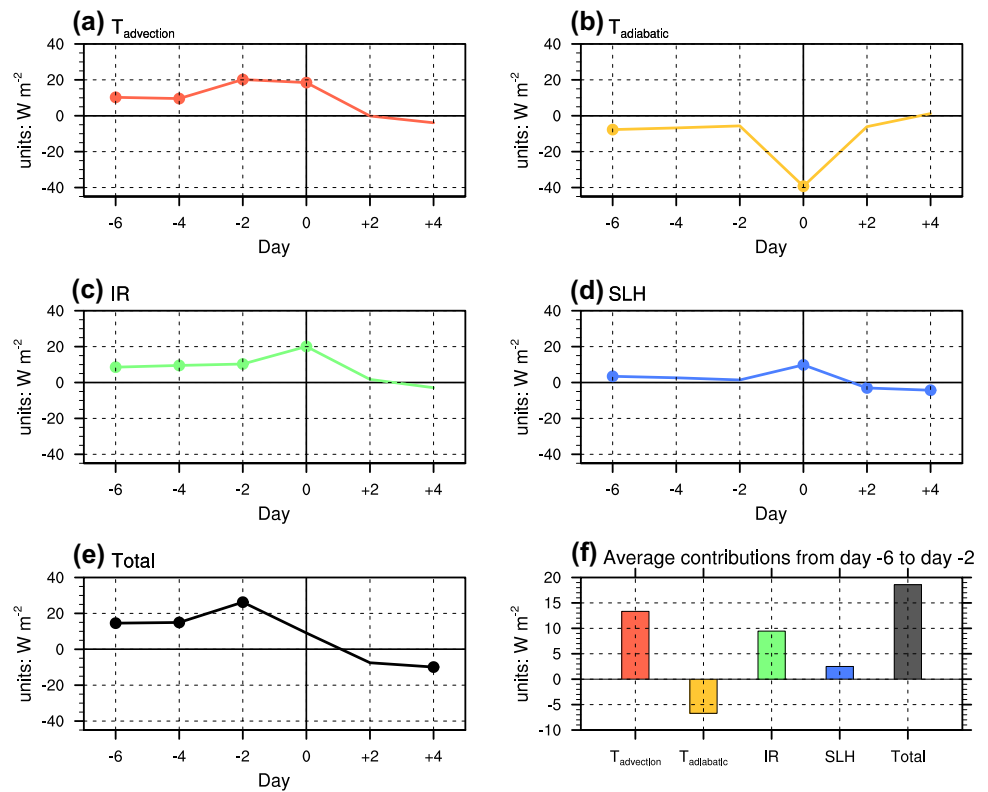
adjacent ocean. The moisture flux across the southeastern coastal boundary is divided into zonal and meridional components. The zonal/meridional component of the moisture flux is calculated as the sum of moisture fluxes across the eastern/southern boundaries (blue/green lines in Fig. S6) of all the grid cells along the southeastern coastal boundary. Therefore, the zonal and meridional components of the moisture flux across the southeast coastline can be viewed as the moisture flux across an eastern boundary and a southern boundary of South China.

Figure 11 displays the time evolution of the contributions of the three terms on the right hand of Eq. (5) for the blocking precipitation events. Both of the water vapor transport terms (the second term; the sum of the vertically-integrated moisture fluxes across the four boundaries of South China; black line in Fig. 11a) and local evaporation (the third term; orange line in Fig. 11a) made positive contributions to moisture over South China throughout the period from day − 6 to day + 4. On day − 2, the water vapor transport reached its peak, which was nearly double the contribution from local evaporation. However, the extreme precipitation events did not appear on day − 2, mainly because the moisture increase due to water vapor transport transformed into the precipitable water (the first term; green line in Fig. 11a, b). On day 0, in spite of the reduction in the water vapor transport, the extreme precipitation events were initiated, primarily due to the condensation

of precipitable water. The reduction of precipitable water on day 0 was closely related to the approach of the cold anomalies (Fig. 8g), which weakened the moisture holding capacity of the atmosphere. Apart from a slight enhancement due to the wetter land surface after the onset of the precipitation events, the local evaporation was relatively constant throughout the period from day − 6 to day + 4 (orange line in Fig. 11a, b).

Figure 11c, e illustrates the time evolution of the water vapor transport across the four boundaries. Throughout the period from day − 6 to day + 4, in blocking precipitation events, the water vapor transport across the southern and western boundaries made positive contributions to the moisture increase over South China, while the contributions across the northern and eastern boundaries were negative. On nearly all the days from day − 6 to day + 4 with the exception of day 0, the water vapor transport across the western boundary exceeded that across the southern boundary. At day 0, the water vapor transport across the southern boundary increased rapidly, due to the eastward movement of the cyclonic anomalies (with southwesterly wind anomalies on their eastern edge) prior to the onset of the precipitation events (Fig. S5b). Correspondingly, the water vapor transport across the eastern boundary also intensified dramatically on day 0. Because the increase in the water vapor transport across the southern boundary was nearly offset by that across the eastern boundary, the peak in the net water
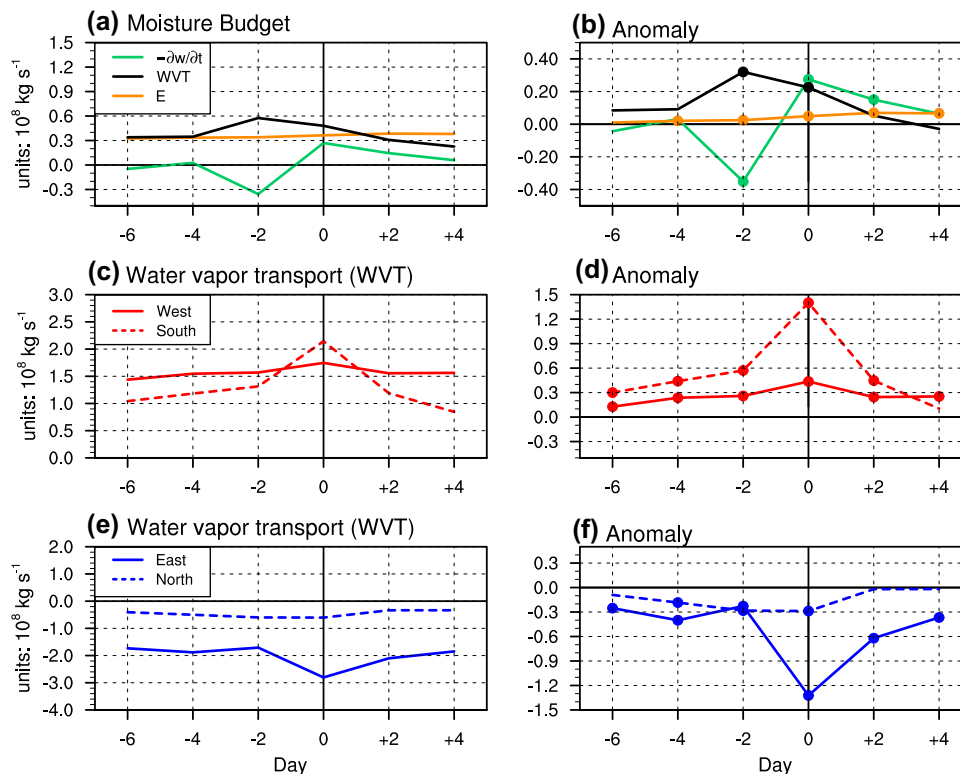
Fig. 11 Time evolution of **a** contributions to the precipitation by three physical processes, i.e., the local rate of precipitable water ($-\frac{\partial w}{\partial t}$; units: 10^8 kg s^{-1}), convergence of the vertically-integrated water vapor transports (WVT; units: 10^8 kg s^{-1}) and evaporation (E; units: 10^8 kg s^{-1}), **c** the vertically-integrated water vapor transports (units: 10^8 kg s^{-1}) across the western and southern boundaries, and **e** the vertically-integrated water vapor transports (units: 10^8 kg s^{-1}) across the eastern and northern boundaries from day -6 to day $+4$ (with an interval of 2 days) for the 141 extreme precipitation events with pre-existing European blocking highs. The anomalies for the quantities in **a**, **c**, and **e** relative to the average during DJF 1979–2013 are given in **b**, **d**, and **f**. In panels **b**, **d**, and **f**, the composite value with a P value not exceeding 0.05 based on the two-tailed Student's *t* tests is denoted by a dot

vapor transport across the regional boundaries appeared on day -2 rather than on day 0 (black line in Fig. 11a).

A lag correlation between the area-averaged sea level pressure anomalies over South China (the sign has been reversed) and the vertically-integrated water vapor fluxes and their divergence during DJF 1979–2013 is conducted to understand the impact of the cyclonic anomaly on the water vapor transport (Fig. 12). About two days before the cyclonic anomaly reached its peak over South China, there were weak, but significant moisture convergences (with negative correlations of $-0.2 \sim -0.1$) over the northern part of South China and the adjacent ocean (Fig. 12c). Meanwhile, there were also significant southwesterly water vapor transports (the magnitude of the correlation coefficient is $\sim$ 0.3) emanating from southeastern Asia and the South China Sea into South China. As the cyclonic anomaly over South China reached its peak, these southwesterly water vapor transports reached their maximum (Fig. 12d) and the correlation between the cyclonic anomaly and the moisture convergence over South China and adjacent ocean also reached their peaks ($-0.4 \sim -0.3$), indicating they were highly

synchronized. After the cyclonic anomaly peaked, the intensity of the southwesterly water vapor transport significantly weakened, and the area of moisture convergence retreated to the adjacent ocean (Fig. 12e, f).

The correlations between the area-averaged sea level pressure anomalies over South China (the sign has been reversed) and the water vapor transports across the four boundaries of South China and their sum were calculated for blocking precipitation events on day 0. The correlation coefficients for the 141 blocking type precipitation events were 0.20 (western), 0.44 (southern), -0.28 (eastern), -0.37 (northern), and 0.18 (the sum of the four boundaries), all of which were significant at 95% confidence level. Therefore, the presence of the cyclonic anomalies was conducive to the moisture increase over South China by the water vapor transport across the western and southern boundaries and was favorable to the moisture decrease by the water vapor transport across the eastern and northern boundaries. The net effect of the cyclonic anomalies over South China was conducive to the moisture convergence and thus the extreme precipitation over South China.

Fig. 12 Correlation coefficients between the area-averaged sea level pressure anomaly over the land areas of South China (105–123°E, 20–32°N) and the vertically-integrated water vapor transports (vector) and their divergence (shading) during DJF 1979–2013, when the water vapor transports and their divergence lead the sea level pressure anomalies by **a** + 6 days, **b** + 4 days, **c** + 2 days, **d** 0 days, **e** − 2 days, and **f** − 4 days. The sign of the sea level pressure anomaly is reversed to emphasize the relationship between the cyclonic anomaly and the water vapor transport. Only the values that meet the 95% confidence level based on two-tailed Student's *t* tests are plotted. Vector is plotted if the vertically-integrated water vapor transports are significant in at least one direction (zonal or meridional)
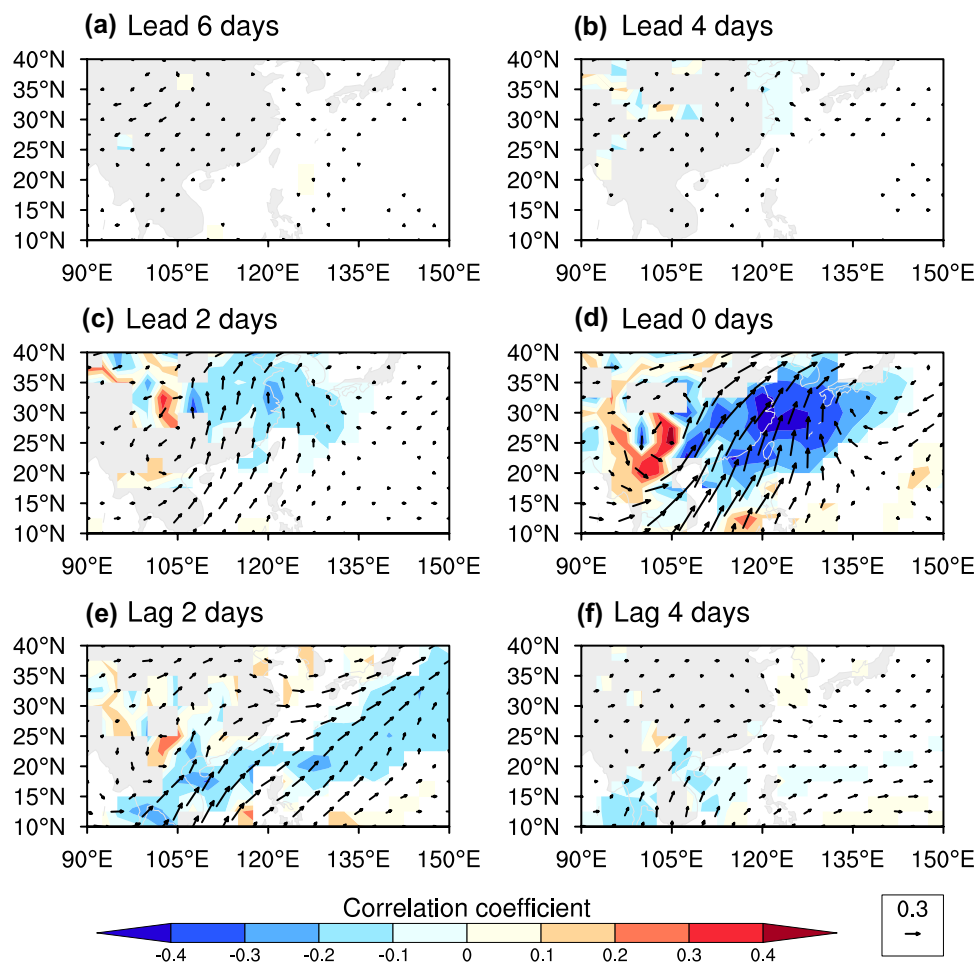
7 Summary and concluding remarks

Based on the precipitation data from 770 surface stations within South China, 183 extreme precipitation events were identified during the study period. It was determined that cyclonic anomalies over South China play an essential role in the formation of extreme precipitation events through the strengthening of updrafts and horizontal moisture convergence.

Composite analysis of circulation anomalies in the upper troposphere (300 hPa) reveals that a European blocking event often preceded the formation of such a cyclonic anomaly over South China, with a lead time of about 10 days. Using an atmospheric blocking tracking algorithm, it is found that 141 extreme precipitation events (about 77% of the total) were preceded by European blocking events. The formation mechanism for these 141 extreme precipitation events has been explored. The generation and downstream propagation of wave activity fluxes organized a Rossby wave train consisting anticyclonic anomalies over Western Europe and the Arabian Sea, along with cyclonic anomalies downstream of the blocking high over Western Europe and cyclonic anomalies over East Asia. The spatial pattern of the circulation anomalies in this Rossby wave train evoked the positive phase of the circumglobal teleconnection.

In addition to the role played by remote circulation anomalies, local surface temperature anomalies also contributed to the development of blocking-type precipitation events. In the lead-up to blocking-type events, warm anomalies emerged over South China with a lead time of 6 days. A heat budget analysis reveals that these warm surface air temperature anomalies originated mainly because of warm advection downstream of the cyclonic anomalies and enhanced downward long-wave fluxes due to the formation of clouds. The presence of near-surface warm anomalies supported a build-up of water vapor in the lower atmosphere. As a consequence, moisture increases due to large-scale convergence and local evaporation drove an increase in precipitable water rather than immediate precipitation. A moisture budget analysis suggests that the moisture for these extreme precipitation events entered South China mainly across the western and southern boundaries. Further, cold anomalies arrived in South China from the north around the onset of the extreme precipitation events. These cold anomalies displaced warm,

moist air upward and reduced the overall moisture holding capacity of the atmosphere, leading to the occurrence of extreme precipitation.

Our study is distinguished from previous synoptic perspective studies (Zong et al. 2014; Lou et al. 2017; Ding and Li 2017) that focused on the extreme precipitation events over South China in the following aspects: First, our study considers not only the 38 persistent extreme precipitation events with lifetimes ≥ 3 days, but also the 145 short-lived extreme precipitation events with lifetimes < 3 days. Therefore, the conclusions drawn from this study apply to extreme precipitation events of any duration. Second, in the previous studies, extreme precipitation events were found to be primarily triggered by a Rossby wave train associated with anticyclonic anomalies over the Arabian Sea, and the role of European blocking was not emphasized. In our study, the Rossby wave train was found to only associated with scatted anticyclonic anomalies over the Arabian Sea. By contrast, our study reveals that the European blocking plays the dominant role in the formation of the majority of extreme precipitation events over South China. Third, in our study, pre-existing warm anomalies and rapid near-surface temperature drops are found to play important roles in the formation of extreme precipitation events. These features were not identified or examined by the previous studies.

It is important to note that most of the severe cold surges over East Asia (including South China) are usually triggered by the Ural blocking events (Cheung et al. 2013, 2015; Luo et al. 2016a, b; Yang et al. 2017). Therefore, while the European and Ural blocking events occur over different upstream regions, we can conclude that the blocking activities upstream of South China favored both extreme precipitation events and severe cold surges over South China.

We have classified precipitation events into two types in this paper based on the existence or absence of a blocking high over Western Europe, and examined the mechanisms behind the 77% of these events that were preceded by blocking highs over Western Europe. This does not preclude the other perspectives for exploring the possible formation mechanisms. We could also classify the precipitation events under consideration into different types according to: (1) the existence of pre-existing warm surface temperature anomalies over South China; (2) the existence of a sharp temperature front during the precipitation event; (3) the intensity of the pre-existing Siberian High; (4) the moisture sources for the precipitation, or the other perspectives. Exploring the formation of the precipitation events from these perspectives may further promote our understanding and improve the predictability of the wintertime extreme precipitation events over South China.

References

Ashok K, Behera SK, Rao SA, Weng H, Yamagata T (2007) El Niño Modoki and its possible teleconnection. J Geophys Res Oceans. https://doi.org/10.1029/2006JC003798

Barriopedro D, García-Herrera R, Lupo AR, Hernández E (2006) A climatology of Northern Hemisphere blocking. J Clim 19(6):1042–1063. https://doi.org/10.1175/JCLI3678.1

Branstator G (2002) Circumglobal Teleconnections, the Jet Stream Waveguide, and the North Atlantic Oscillation. J Clim 15(14):1893–1910. https://doi.org/10.1175/1520-0442(2002)0151893:CTTJSW2.0.CO;2

Bueh C, Shi N, Xie Z (2011) Large-scale circulation anomalies associated with persistent low temperature over Southern China in January 2008. Atmos Sci Let 12(3):273–280. https://doi.org/10.1002/asl.333

Cheung HHN, Zhou W, Lee SM, Tong HW (2015) Interannual and interdecadal variability of the number of cold days in Hong Kong and their relationship with large-scale circulation. Mon Wea Rev 143(4):1438–1454. https://doi.org/10.1175/MWR-D-14-00335.1

Cheung HN, Zhou W, Mok HY, Wu MC (2012) Relationship between Ural-Siberian Blocking and the East Asian winter monsoon in relation to the Arctic oscillation and the El Niño–Southern oscillation. J Clim 25(12):4242–4257. https://doi.org/10.1175/JCLI-D-11-00225.1

Cheung HN, Zhou W, Shao Y, Chen W, Mok HY, Wu MC (2013) Observational climatology and characteristics of wintertime atmospheric blocking over Ural-Siberia. Clim Dyn 41(1):63–79. https://doi.org/10.1007/s00382-012-1587-6

Choi JW, Lee SW, Lim BH, Kim BJ (2016) Interdecadal change of winter precipitation over Southern China in Late 1990s. J Meteor Soc Japan Ser II 94(2):197–213. https://doi.org/10.2151/jmsj.2016-011

Davini P, Cagnazzo C, Gualdi S, Navarra A (2012) Bidimensional diagnostics, variability, and trends of Northern Hemisphere blocking. J Clim 25(19):6496–6509. https://doi.org/10.1175/JCLI-D-12-00032.1

Davini P, Cagnazzo C, Fogli PG, Manzini E, Gualdi S, Navarra A (2014) European blocking and Atlantic jet stream variability in the NCEP/NCAR reanalysis and the CMCC–CMS climate model. Clim Dyn 43(1):71–85. https://doi.org/10.1007/s00382-013-1873-y

Diao Y, Li J, Luo D (2006) A new blocking index and its application: blocking action in the Northern Hemisphere. J Clim 19(19):4819–4839. https://doi.org/10.1175/JCLI3886.1

Ding F, Li C (2017) Subtropical westerly jet waveguide and winter persistent heavy rainfall in South China. J Geophys Res Atmos. https://doi.org/10.1002/2017JD026530

Feldstein SB, Dayan U (2008) Circumglobal teleconnections and wave packets associated with Israeli winter precipitation. Q J R Meteor Soc 134(631):455–467. https://doi.org/10.1002/qj.225

Feng J, Wang L, Chen W, Fong SK, Leong KC (2010) Different impacts of two types of Pacific Ocean warming on Southeast Asian rainfall during boreal winter. J Geophys Res Atmos. https://doi.org/10.1029/2010JD014761

Held IM, Soden BJ (2006) Robust responses of the hydrological cycle to global warming. J Clim 19(21):5686–5699. https://doi.org/10.1175/JCLI3990.1

Hong CC, Li T (2009) The extreme cold anomaly over Southeast Asia in February 2008: roles of ISO and ENSO. J Clim 22(13):3786–3801. https://doi.org/10.1175/2009JCLI2864.1

Hu A, Xie W, Li N, Xu X, Ji Z, Wu J (2014) Analyzing regional economic impact and resilience: a case study on electricity outages caused by the 2008 snowstorms in southern China. Nat Hazards 70(2):1019–1030. https://doi.org/10.1007/s11069-013-0858-9

Hu K, Huang G, Wu R, Wang L (2017) Structure and dynamics of a wave train along the wintertime Asian jet and its impact on East Asian climate. Clim Dyn. https://doi.org/10.1007/s00382-017-3674-1

Huang D, Dai A, Zhu J, Zhang Y, Kuang X (2017) Recent winter precipitation changes over Eastern China in different warming periods and the associated East Asian jets and oceanic conditions. J Clim 30(12):4443–4462. https://doi.org/10.1175/JCLI-D-16-0517.1

Huang W, Wang B, Wright JS (2016) A potential vorticity-based index for the East Asian winter monsoon. J Geophys Res Atmos 121(16):9382–9399. https://doi.org/10.1002/2016JD025053

Jeong JH, Ho CH (2005) Changes in occurrence of cold surges over east Asia in association with Arctic Oscillation. Geophys Res Lett. https://doi.org/10.1029/2005GL023024

Jia X, Ge J (2017) Interdecadal changes in the relationship between ENSO, EAWM, and the wintertime precipitation over China at the end of the twentieth century. J Clim 30(6):1923–1937. https://doi.org/10.1175/JCLI-D-16-0422.1

Kalnay E, Kanamitsu M, Kistler R, Collins W, Deaven D, Gandin L, Iredell M, Saha S, White G, Woollen J, Zhu Y, Leetmaa A, Reynolds R, Chelliah M, Ebisuzaki W, Higgins W, Janowiak J, Mo KC, Ropelewski C, Wang J, Jenne R, Joseph D (1996) The NCEP/NCAR 40-year reanalysis project. Bull Am Meteor Soc 77(3):437–471. https://doi.org/10.1175/1520-0477(1996)077<0437:TNYRP>2.0.CO;2

Leung MYT, Cheung HHN, Zhou W (2015) Energetics and dynamics associated with two typical mobile trough pathways over East Asia in boreal winter. Clim Dyn 44(5):1611–1626. https://doi.org/10.1007/s00382-014-2355-6

Li Q, Yang S, Kousky VE, Higgins RW, Lau KM, Xie P (2005) Features of cross-Pacific climate shown in the variability of China and US precipitation. Int J Climatol 25(13):1675–1696. https://doi.org/10.1002/joc.1271

Li X, Zhou W (2016) Modulation of the interannual variation of the India-Burma Trough on the winter moisture supply over Southwest China. Clim Dyn 46(1):147–158. https://doi.org/10.1007/s00382-015-2575-4

Li X, Zhou W, Chen YD (2016) Detecting the origins of moisture over southeast china: Seasonal variation and heavy rainfall. Adv Atmos Sci 33(3):319–329. https://doi.org/10.1007/s00376-015-4197-5

Li XF, Li J, Li Y (2015) Recent winter precipitation increase in the Middle-Lower Yangtze River Valley since the Late 1970s: a response to warming in the Tropical Indian Ocean. J Clim 28(9):3857–3879. https://doi.org/10.1175/JCLI-D-14-00701.1

Lin CA, Stewart RE (1986) Mesoscale circulations initiated by melting snow. J Geophys Res Atmos 91(D12):13,299–13,302. https://doi.org/10.1029/JD091iD12p13299

Lou M, Li C, Hao S, Liu J (2017) Variations of winter precipitation over Southeastern China in association with the North Atlantic Oscillation. J Meteorol Res 31(3):476. https://doi.org/10.1007/s13351-017-6103-9

Luo D, Xiao Y, Yao Y, Dai A, Simmonds I, Franzke CLE (2016a) Impact of Ural blocking on winter warm Arctic-Cold Eurasian anomalies. Part I: Blocking-induced amplification. J Clim 29(11):3925–3947. https://doi.org/10.1175/JCLI-D-15-0611.1

Luo D, Xiao Y, Diao Y, Dai A, Franzke CLE, Simmonds I (2016b) Impact of Ural blocking on winter warm Arctic–Cold Eurasian anomalies. Part II: The Link to the North Atlantic Oscillation. J Clim 29(11):3949–3971. https://doi.org/10.1175/JCLI-D-15-0612.1

Nan S, Zhao P (2012) Snowfall over central-eastern China and Asian atmospheric cold source in January. Int J Climatol 32(6):888–899. https://doi.org/10.1002/joc.2318

O'Gorman PA, Muller CJ (2010) How closely do changes in surface and column water vapor follow Clausius-Clapeyron scaling in climate change simulations? Environ Res Lett. https://doi.org/10.1088/1748-9326/5/2/025207

Park TW, Ho CH, Deng Y (2014) A synoptic and dynamical characterization of wave-train and blocking cold surge over East Asia. Clim Dyn 43(3):753–770. https://doi.org/10.1007/s00382-013-1817-6

Plumb RA (1985) On the three-dimensional propagation of stationary waves. J Atmos Sci 42(3):217–229. https://doi.org/10.1175/1520-0469(1985)042<0217:OTTDPO>2.0.CO;2

Shine KP (1984) Parametrization of the shortwave flux over high albedo surfaces as a function of cloud thickness and surface albedo. Q J R Meteorol Soc 110(465):747–764. https://doi.org/10.1002/qj.49711046511

Su W, Zhang X, Wang Z, Su X, Huang J, Yang S, Liu S (2011) Analyzing disaster-forming environments and the spatial distribution of flood disasters and snow disasters that occurred in China from 1949 to 2000. Math Comput Model 54(3):1069–1078. https://doi.org/10.1016/j.mcm.2010.11.037

Szeto KK, Lin CA, Stewart RE (1988) Mesoscale circulations forced by melting snow. Part I: Basic simulations and dynamics. J Atmos Sci 45(11):1629–1641. https://doi.org/10.1175/1520-0469(1988)045<1629:MCFBMS>2.0.CO;2

Takaya K, Nakamura H (2001) A formulation of a phase-independent wave-activity flux for stationary and migratory Quasigeostrophic Eddies on a zonally varying basic flow. J Atmos Sci 58(6):608–627. https://doi.org/10.1175/1520-0469(2001)058<0608:AFOAPI>2.0.CO;2

Takaya K, Nakamura H (2005) Geographical dependence of upper-level blocking formation associated with intraseasonal amplification of the Siberian high. J Atmos Sci 62(12):4441–4449. https://doi.org/10.1175/JAS3628.1

Tam CY, Li T (2006) The origin and dispersion characteristics of the observed tropical summertime synoptic-scale waves over the Western Pacific. Mon Wea Rev 134(6):1630–1646. https://doi.org/10.1175/MWR3147.1

Tao WK, Lang S, Olson WS, Meneghini R, Yang S, Simpson J, Kummerow C, Smith E, Halverson J (2001) Retrieved vertical profiles of latent heat release using TRMM rainfall products for February 1998. J Appl Meteor 40(6):957–982. https://doi.org/10.1175/1520-0450(2001)040<0957:RVPOLH>2.0.CO;2

Trenberth KE (2011) Changes in precipitation with climate change. Clim Res 47:123–138. https://doi.org/10.3354/cr00953

Trenberth KE, Guillemot CJ (1995) Evaluation of the Global Atmospheric Moisture Budget as Seen from Analyses. J Clim 8(9):2255–2272. https://doi.org/10.1175/1520-0442(1995)008<2255:EOTGAM>2.0.CO;2

Trenberth KE, Dai A, Rasmussen RM, Parsons DB (2003) The changing character of precipitation. Bull Am Meteorol Soc 84(9):1205–1217. https://doi.org/10.1175/BAMS-84-9-1205

Tyrlis E, Hoskins BJ (2008) Aspects of a Northern Hemisphere atmospheric blocking climatology. J Atmos Sci 65(5):1638–1652. https://doi.org/10.1175/2007JAS2337.1

Wang B, Wu R, Fu X (2000) Pacific-East Asian teleconnection: how does ENSO affect East Asian climate? J Clim 13(9):1517–1536. https://doi.org/10.1175/1520-0442(2000)013<1517:PEATHD>2.0.CO;2

Wang L, Chen W (2010) How well do existing indices measure the strength of the East Asian winter monsoon? Adv Atmos Sci 27(4):855–870. https://doi.org/10.1007/s00376-009-9094-3

Wang L, Chen W, Zhou W, Chan JCL, Barriopedro D, Huang R (2010) Effect of the climate shift around mid 1970s on the relationship between wintertime Ural blocking circulation and East Asian climate. Int J Climatol 30(1):153–158. https://doi.org/10.1002/joc.1876

Wen M, Yang S, Kumar A, Zhang P (2009) An Analysis of the Large-Scale Climate Anomalies Associated with the Snowstorms Affecting China in January 2008. Mon Wea Rev 137(3):1111–1131. https://doi.org/10.1175/2008MWR2638.1

Weng H, Behera SK, Yamagata T (2009) Anomalous winter climate conditions in the Pacific Rim during recent El Niño Modoki and El Niño events. Clim Dyn 32(5):663–674. https://doi.org/10.1007/s00382-008-0394-6

Woollings T, Hoskins B, Blackburn M, Berrisford P (2008) A new rossby wave-breaking interpretation of the North Atlantic oscillation. J Atmos Sci 65(2):609–626. https://doi.org/10.1175/2007JAS2347.1

Wu B, Wang J (2002) Winter Arctic oscillation, Siberian high and East Asian Winter monsoon. Geophys Res Lett 29(19):3-1–3-4. https://doi.org/10.1029/2002GL015373

Wu MC, Chan JCL (1995) Surface features of winter monsoon surges over South China. Mon Wea Rev 123(3):662–680. https://doi.org/10.1175/1520-0493(1995)1230662:SFOWMS2.0.CO;2

Wu MC, Chan JCL (1997) Upper-level features associated with winter monsoon surges over South China. Mon Wea Rev 125(3):317–340. https://doi.org/10.1175/1520-0493(1997)1250317:ULFAWW2.0.CO;2

Wu R, Hu ZZ, Kirtman BP (2003) Evolution of ENSO-related rainfall anomalies in East Asia. J Clim 16(22):3742–3758. https://doi.org/10.1175/1520-0442(2003)0163742:EOERAI2.0.CO;2

Xie W, Li N, Li C, Wu Jd, Hu A, Hao X (2014) Quantifying cascading effects triggered by disrupted transportation due to the Great 2008 Chinese Ice Storm: implications for disaster risk management. Nat Hazards 70(1):337–352. https://doi.org/10.1007/s11069-013-0813-9

Yanai M, Tomita T (1998) Seasonal and interannual variability of atmospheric heat sources and moisture sinks as determined from NCEP-NCAR reanalysis. J Clim 11(3):463–482. https://doi.org/10.1175/1520-0442(1998)0110463:SAIVOA2.0.CO;2

Yanai M, Esbensen S, Chu JH (1973) Determination of bulk properties of tropical cloud clusters from large-scale heat and moisture budgets. J Atmos Sci 30(4):611–627. https://doi.org/10.1175/1520-0469(1973)0300611:DOBPOT2.0.CO;2

Yang Z, Huang W, Wang B, Chen R, Wright JS, Ma W (2017) Possible mechanisms for four regimes associated with cold events over East Asia. Clim Dyn. https://doi.org/10.1007/s00382-017-3905-5

Yao S, Huang Q (2016) An analysis of extreme intraseasonal rainfall events during January–March 2010 over eastern China.

Dyn Atmos Oceans 75:22–32. https://doi.org/10.1016/j.dynatmoce.2016.04.001

Yao Y, Luo D, Dai A, Simmonds I (2017) Increased quasi stationarity and persistence of winter Ural Blocking and Eurasian extreme cold events in response to Arctic warming. Part I: Insights from observational analyses. J Clim 30(10):3549–3568. https://doi.org/10.1175/JCLI-D-16-0261.1

Yuan Y, Li C, Yang S (2014) Decadal anomalies of winter precipitation over southern China in association with El Niño and La Niña. J Meteorol Res 28(1):91–110. https://doi.org/10.1007/s13351-014-0106-6

Zhang R, Sumi A (2002) Moisture Circulation over East Asia during El Niño Episode in Northern Winter, Spring and Autumn. J Meteor Soc Japan Ser II 80(2):213–227. https://doi.org/10.2151/jmsj.80.213

Zhang R, Sumi A, Kimoto M (1999) A diagnostic study of the impact of El Niño on the precipitation in China. Adv Atmos Sci 16(2):229–241. https://doi.org/10.1007/BF02973084

Zhang T (2005) Influence of the seasonal snow cover on the ground thermal regime: an overview. Rev Geophys. https://doi.org/10.1029/2004RG000157

Zhang Y, Sperber KR, Boyle JS (1997) Climatology and interannual variation of the East Asian Winter Monsoon: results from the 1979–95 NCEP/NCAR reanalysis. Mon Wea Rev 125(10):2605–2619. https://doi.org/10.1175/1520-0493(1997)1252605:CAIVOT2.0.CO;2

Zhou B, Gu L, Ding Y, Shao L, Wu Z, Yang X, Li C, Li Z, Wang X, Cao Y, Zeng B, Yu M, Wang M, Wang S, Sun H, Duan A, An Y, Wang X, Kong W (2011) The great 2008 Chinese ice storm: its socioeconomic-ecological impact and sustainability lessons learned. Bull Am Meteorol Soc. https://doi.org/10.1175/2010bams2857.1

Zhou LT, Wu R (2010) Respective impacts of the East Asian winter monsoon and ENSO on winter rainfall in China. J Geophys Res Atmos 115(D2): https://doi.org/10.1029/2009JD012502

Zhou LT, Tam CY, Zhou W, Chan JCL (2010) Influence of South China Sea SST and the ENSO on winter rainfall over South China. Adv Atmos Sci 27(4):832–844. https://doi.org/10.1007/s00376-009-9102-7

Zhou W, Chan JCL, Chen W, Ling J, Pinto JG, Shao Y (2009) Synoptic-scale controls of persistent low temperature and Icy weather over Southern China in January 2008. Mon Wea Rev 137(11):3978–3991. https://doi.org/10.1175/2009MWR2952.1

Zong H, Bueh C, Ji L (2014) Wintertime extreme precipitation event over southern China and its typical circulation features. Chin Sci Bull 59(10):1036–1044. https://doi.org/10.1007/s11434-014-0124-x